Three-dimensional particle size and position measurement by linear complex amplitude Wiener filtering

Marina Gómez-Climente, [ID] Julia Lobera Salazar, [ID] Maria Pilar Arroyo de Grandes, [ID] and Virginia Palero Díaz[*] [ID]

Instituto de Investigación en Ingeniería de Aragón (I3A), Universidad de Zaragoza, C/ Mariano Esquillor s/n, 50018 Zaragoza, Spain
[*]*palero@unizar.es*

Abstract: Digital in-line holography (DIH) combined with a Wiener filter has been applied to measure particle size and position in the flow inside a capillary model, seeded with magnetic particles (3μm) and with solid opaque particles that simulated red and white cells. The proposed filtering process takes advantage of the linearity implicit in the numerical reconstruction of the object complex amplitude. A modified DIH set-up, with a tilted illumination beam, was used as it presents two main advantages: it solves the twin image issue associated to in-line holography and increases the out-of-plane resolution. Experiments show that the proposed method discriminates particles within a range from 3 to 30μm with a sensitivity of 0.5μm.

1. Introduction

The measurement of the size and position of solid and fluid particles (as droplets or bubbles) is essential for a broad range of applications in fields such as pharmacy, biomedicine or chemistry. In the treatment of some diseases, such as cancer, the patient sometimes suffers from side effects, as the chemotherapy can damage not only harmful cells but also the healthy ones. These side effects could be avoided if the medication could be taken to the exact point where treatment is needed. A possibility comes from the use of functionalized magnetic particles coated with drugs that can be guided through the circulatory system by an external magnetic field [1–4]. In order to develop realistic models of the transport and accumulation of these particles in capillaries, veins and arteries, their interaction with other substances in the blood must be known. Thus, we need to combine different techniques in order to obtain complete information from all the particles and to distinguish the magnetic particles from cells in the bloodstream such as white and red cells or platelets, among others. These methods should address the location of different particles in a volume (3D space) and measure their entire velocity field. This is one example among many, which highlights the need to develop combined techniques to determine the position, velocity and size of particles, droplets and bubbles.

Digital In-line Holography (DIH) is a well-known 3D technique that allows the recording and reconstruction of an object complex amplitude distribution [5,6]. It has been applied to the measurement of three-dimensional velocity fields [7–9], particle distributions [10–12] and particle sizes [13–16].

DIH has been applied in some works with a modified set-up which is often referred to as sideband holography [17–20]. In this configuration, the object is imaged near the sensor plane with a lens. The advantage of introducing a lens in the classical DIH set-up is double. First, the lens allows modifying the magnification and, therefore, adjusting the recorded field of view. Second, it allows solving the twin image issue by recording only half of the object power spectrum, while blocking the other half, without losing any information. This is done by placing an aperture in the lens focal plane. So, a lensless Fourier hologram of the unblocked spectrum is produced.

The hologram Fourier transform will show the real and virtual images of the unblocked spectrum separated, as in an off-axis configuration. This set-up introduces several advantages when applied to the measurement of the 3D velocity field of a particle distribution which outperform the decrease in the transversal resolution associated to the reduced power spectrum. One of them is the improvement in the measurement of the small out-of-plane displacements that are otherwise underestimated [21].

However, the main limitation in the accuracy of the measured 3D velocity field is the location and tracking of the particle along the optical axis direction. The axial resolution depends not only on the frequencies recorded, but also on the illumination and observation directions, as it has been recently demonstrated in [20].

In the present work, the sideband set-up will be used introducing a further modification, by tilting the illumination angle as in [20]. There, the authors show that illuminating a particle field with one single tilted collimated beam and using a rectangular aperture in the lens focal plane, centered on the optical axis, improves more than a 17% the position and a 32% the displacements measured with a parallel illumination and a displaced aperture as in [18].

When DIH is applied to measure the location and velocity of any particle distribution, it is generally combined with Particle Tracking Velocimetry (PTV). The location algorithms used for PTV [22,23] consider particles as point scatterers whose scattering pattern present a nice local intensity maximum. However, particle scattering depends on its size [24] and may present a complex structure with several local maxima. Besides, depending on the size distribution and particle density, the individual particle scattering intensity can be affected by multiple scattering, the overlapping of the scattering of different particles, and even by the mean illumination direction.

In order to make an efficient and correct use of the PTV algorithms, the most desirable scenario is to have particles that behave as point scatterers. If it is not the case, one possibility is to turn the particles images into point scatterers to correctly locate and track them. This can be achieved by using Matched Filters that produce a delta function when the detected structure matches the filter. Matched filters present a great potential [25] and have been used to calculate the cross correlation in velocimetry [26], to reduce the noise in velocity fields [27,28] or to improve the particle location [29–31]. We can take advantage of the application of a Matched Filter, for example a Wiener Filter (WF), and turn the complicated scattering of a particle of a given diameter in a delta-ish distribution. An improvement in the performance of the PTV algorithm is expected in addition to obtaining information on the size of the particles.

The objective of this paper is to measure simultaneously the size and position of opaque particles with different size, density and coating in the volume of a capillary model by applying a Wiener Filter in a DIH set-up. As far as we know, this is the first time that the Wiener filter is used as a particle sizing tool. The proposed filtering process is also new: it takes advantage of the linearity implicit in the numerical reconstruction of the object complex amplitude, which reduces considerably the computation time when big volumes are recorded. A preliminary work [32] showed promising results when discriminating particles with two very different sizes. In this work, we address a much more complex problem by dealing with a broader and continuous size range, which has led us to develop an iterative process that can be applied to any particle field.

We will start by setting the theoretical bases of this work. Next, we will describe the modified sideband DIH set-up and the procedure followed to measure the particle size and position. We will analyze the challenge faced when particles with different sizes are holographically recorded and reconstructed. We will use a specific 2D representation of the complex 3D particle scattering to better visualize the filtering performance. In the next section, we will analyze the Wiener filter performance and its application to the reconstructed object complex amplitude. In the last section, the results of applying the 3D filtering method to different flow models and to a real flow will be shown.

2. Theoretical filter definition and linear application

The complex amplitude of the object scattered field at a position given by , can be expressed as a function of its spectral components, $S(\vec{k})$, as [33–35]:

$$U_o(\vec{r}) = \int_{-\infty}^{+\infty} S(\vec{k}) \exp(i\vec{k} \cdot \vec{r}) d\vec{k}, \tag{1}$$

where $\vec{k} = (k_x, k_y, k_z)$ is the wave vector. As the object scattering is measured at the far field, only the propagating plane-waves, with a wave number $|\vec{k}| = 2\pi/\lambda$, are recorded. This reduces the measured spectral components to a spherical surface in the k-space, which implies that $\vec{k}$ has only two independent variables, as $k_z = \sqrt{k^2 - (k_x^2 + k_y^2)}$. Besides, the objet recorded scattering is further limited by the numerical aperture [33–35]. In such a case $S(\vec{k})$ becomes a two-dimensional matrix. For clarity, from now on we will denote two-dimensionality by using a tilde. Then,

$$\tilde{S}(\vec{k}) = S\left(k_x, k_y, \sqrt{k^2 - (k_x^2 + k_y^2)}\right). \tag{2}$$

Thus, in the hologram plane, placed at $\vec{r}_o = (x, y, 0)$, the two-dimensional complex amplitude of the object can be expressed as:

$$\tilde{U}_o(\vec{r}_o) = \int_{-\infty}^{+\infty} \tilde{S}(\vec{k}) \exp(i\vec{k} \cdot \vec{r}_o) d\vec{k}. \tag{3}$$

In the object wave reconstruction, the k-components at any other plane are modified by the transfer function, $H(\vec{k})$, defined as:

$$H(\vec{k}) = \frac{\exp(ik \cdot |\vec{r} - \vec{r}_o|)}{ik|\vec{r} - \vec{r}_o|}. \tag{4}$$

Thus, the object complex amplitude is given by [36]:

$$U_o(\vec{r}) = \int_{-\infty}^{+\infty} \tilde{S}(\vec{k}) H(\vec{k}) \exp(i\vec{k} \cdot \vec{r}) d\vec{k}. \tag{5}$$

By introducing the appropriated frequency filter, $\tilde{F}(\vec{k})$, the spectrum can be modified to enhance the object contrast or, as we propose in this work, to discriminate particles. The object filtered complex amplitude can be written as:

$$U_{oF}(\vec{r}) = \int_{-\infty}^{+\infty} \tilde{S}(\vec{k}) \tilde{F}(\vec{k}) H(\vec{k}) \exp(i\vec{k} \cdot \vec{r}) d\vec{k}. \tag{6}$$

If the object under study is a single particle Eq. (5) turns into

$$U_P(\vec{r}) = \int_{-\infty}^{+\infty} \tilde{P}(\vec{k}) H(\vec{k}) \exp(i\vec{k} \cdot \vec{r}) d\vec{k}, \tag{7}$$

where $\tilde{P}(\vec{k})$ denotes the particle scattering spectral components. Now, the appropriated matched filter will convert the complex scattering pattern of this real particle into the scattering of a punctual particle, which is the ideal scatterer for tracking algorithms. A Wiener Filter ($\tilde{F}_P(\vec{k})$)

has been chosen to this purpose:

$$\tilde{F}_P(\vec{k}) = \frac{\tilde{P}(\vec{k})}{\left|\tilde{P}(\vec{k})\right|^2 + \beta}, \tag{8}$$

where β is a small constant introduced to avoid discontinuities in the filter. If the filter is applied according to Eq. (6), we obtain the particle filtered complex amplitude:

$$U_{PF}(\vec{r}) = \int_{-\infty}^{+\infty} \tilde{P}(\vec{k}) \left(\frac{\tilde{P}(\vec{k})}{\left|\tilde{P}(\vec{k})\right|^2 + \beta} \right) H(\vec{k}) \exp(i\vec{k} \cdot \vec{r}) d\vec{k} \cong \int_{-\infty}^{+\infty} H(\vec{k}) \exp(i\vec{k} \cdot \vec{r}) d\vec{k}. \tag{9}$$

Equation (9) allows us to calculate the filtered complex amplitude at any point in space. At the particle location we will find a maximum, since the integral solution is roughly a delta function.

If the object is a particle field, the filter will provide a delta-like function for every particle that matches the filter. The complex amplitude is then given by:

$$U_{oF}(\vec{r}) = \int_{-\infty}^{+\infty} \tilde{S}_F(\vec{k}) H(\vec{k}) \exp(i\vec{k} \cdot \vec{r}) d\vec{k}, \tag{10}$$

where

$$\tilde{S}_F(\vec{k}) = \tilde{S}(\vec{k}) \tilde{F}_P(\vec{k}). \tag{11}$$

Again, Eq. (10) allows us to reconstruct the complex amplitude of the filtered object, $U_{oF}(\vec{r})$, at any plane. In short, we are modifying the frequency spectrum of the object and propagating the result to any plane in space, taking advantage of the linearity implicit in the numerical reconstruction of the object complex amplitude.

3. Experimental implementation and particle size and position measurement

3.1. Digital sideband holography experimental setup

In this work we use a sideband holographic set-up with a tilted illumination beam [20]. A schematic drawing is presented in Fig. 1(a). The collimated illumination (in green), which is forming an angle $\alpha=10.4°$ with the optical axis, illuminates a generic particle. This angle is determined by the maximum NA allowed by our sensor, which is 0.18. The limiting angles of the particle forward scattering are marked in red.
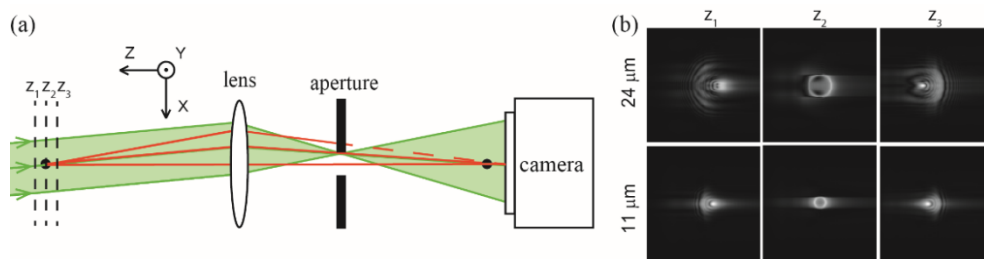

Fig. 1. (a) DIH set-up with tilted illumination and a centered aperture. (b) Simulated absolute value of the scattering pattern of two opaque disks at its focused position (z_2) and in two defocused symmetrical positions: $z_{1,3}=\pm0.1$mm (11µm) and $z_{1,3}=\pm0.16$mm (24µm).

A lens forms the particle image near the camera sensor, slightly out of focus in such a way that the particle diffraction pattern is recorded. A centered aperture blocks half of the power spectrum. This configuration will form a so-called image hologram. However, the presence of

the lens introduces an alternative interpretation of this hologram. In the lens focal plane, the object power spectrum and the illuminating beam, which appears as a bright spot in the center, can be considered as the object beam and the reference beam source, respectively, of a so-called lensless Fourier hologram of the particle distribution spectrum.

Since the recorded interference pattern is a real function, at the Fourier transform of the hologram the particle distribution power spectrum is duplicated. Then, it is possible to record only half of the object power spectrum, while blocking the other half, without losing any information [17,19,20]. This is done by placing an aperture in the lens focal plane. The aperture consists of a non-reflective black sheet, for example, a cardboard, with a cut-out rectangle. The hologram Fourier transform will show the aperture real and virtual images separated, as in an off-axis configuration. In the reconstruction, one of these aperture images is selected, the inverse Fourier Transform is calculated and the resulting complex amplitude distribution is propagated to the plane where the object is in focus.

To understand the challenge of discriminating particles based on their scattering analysis, we will start by numerically simulating the spatial distribution of the particle scattering produced by our DIH set-up.

In Fig. 1(b), we show the absolute value of the scattering pattern,$|U_P(\vec{r})|$, obtained for two opaque disks with diameters of 11μm and 24μm, respectively. In particular, the cross-sections at three different XY planes are shown: in the focused plane (z_2) and in two symmetrical, slightly defocused positions ($z_{1,3}=\pm0.1$mm for the 11μm disk, $z_{1,3}=\pm0.16$mm for the 24μm disk). These images show a broad structure in the plane where the particle is in focus, while a clear maximum appears in the chosen defocused planes. We have found that, for our magnification (M = 7), those maxima always appear for opaque particles with diameters bigger than 7μm. In all cases, the presence of these local maxima will mislead the particle location.

The Wiener filter strategy will be applied to discriminate particles with different sizes in a borosilicate squared-sectioned capillary ($1\times1\times50$mm^3) filled with a mixture of glycerin and water (60/40 in weight). The liquid was seeded with three different particle sets: magnetic particles (MagP-NH$_2$, 2-4μm in diameter, 3μm mean diameter) and two types of non-magnetic particles that are going to simulate, in a first approach, red and white blood cells. Red cells have a diameter between 6 and 8μm, while white cells have a diameter between 8 and 20μm. The offer of non-magnetic seeding particles available is huge. However, they must fulfill several criteria, as not only the particle size and scattering properties, but also its density and its ability in following the flow, are important. We chose silver-coated hollow glass microspheres with a density of 0.67g/ml and 10-20μm diameter, and white polyethylene microspheres with a density of 1.25g/ml and 20-27μm diameter as they meet reasonably well all constrains. For convenience, we will name from now on these particles as red and white cell model, as their mean diameter (given by the manufacturer) are 11μm and 24μm respectively. The capillary model is illuminated with a collimated laser beam (λ= 515nm). A lens (f'=55mm) images the capillary near the sensor of a digital camera (pco.edge, CMOS, 6.5μm/pixel, 2560×2160 pixels). A centered aperture (15.06×29.67mm^2) [18,20] is placed at the lens focal plane. Holograms were recorded when the flow was nearly stopped. To enhance the signal-to-noise ratio (SNR), series of 200 holograms at 33fps (magnetic particles) or 20fps (red and white cell model), were also recorded and their average was subtracted to every hologram. The magnification, M, was set to 7.0, so the capillary recorded length was 2.4mm.

The particle size and position measurement is done in two steps, represented in Figs. 2 and 3. The first step includes the Wiener filter generation and its application to the hologram. The second step provides the position of the particle.
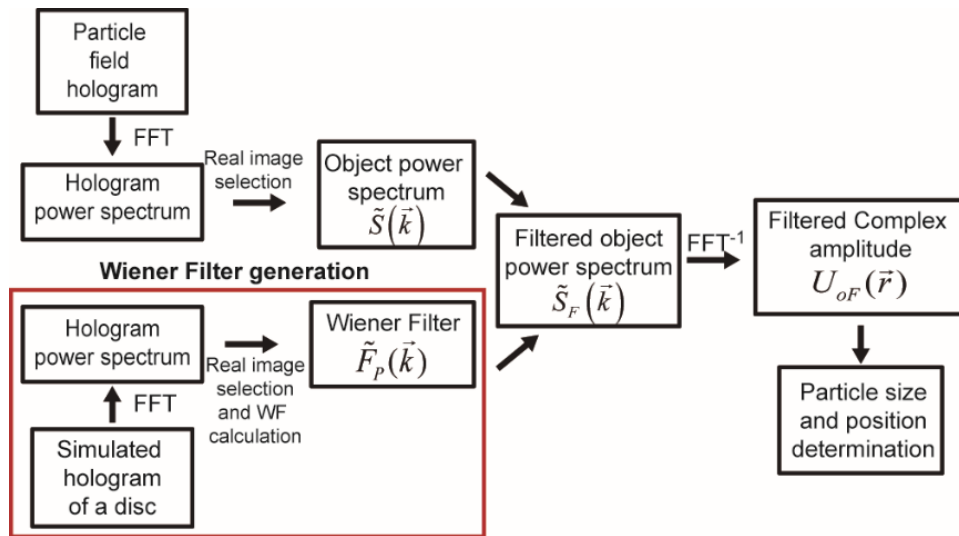
Fig. 2. Flowchart depicting the filtering process, including the generation of the Wiener filter and its application to a hologram
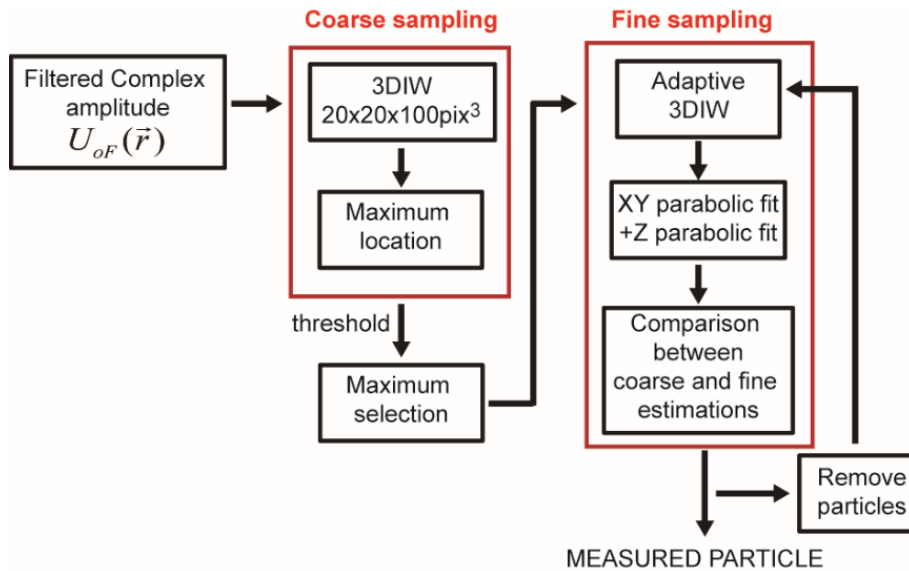
Fig. 3. Flowchart depicting the particle position measurement.

3.2. Wiener filtering experimental application

In order to compute the WF (Wiener Filter generation, Fig. 2), we will start by simulating the diffraction pattern of a disk of a given diameter and its holographic recording as if the disk were recorded with our experimental set-up. We will calculate its Fourier transform, by means of a Fast Fourier Transform (FTT) algorithm, select the aperture real image and compute the 2D WF according to Eq. (8), thus obtaining $\tilde{F}_P(\vec{k})$.

Then, the object power spectrum, $\tilde{S}(\vec{k})$, is obtained by calculating the Fourier transform of the particle field hologram and selecting the aperture real image. We choose to apply the filter before propagating, by multiplying the object power spectrum by the WF. The filtered complex amplitude ($U_{oF}(\vec{r})$) is obtained by calculating the inverse Fourier transform.

With a more standard approach, we would compute the inverse Fourier transform of the object power spectrum and propagate it to obtain the 3D object complex amplitude (Eq. (5)). In the same way, we would also compute the particle model complex amplitude (Eq. (7)) and, from that data, a 3D WF. This option does not present any performance advantage as shown in the next section and it implies to store and work with very large matrices. In addition, as shown in [31], the filtering of the 3D object image should be performed on the 3D intensity distribution; if performed on the 3D complex amplitude, the axial position information will be lost. In our implementation we keep the axial position information as we first apply the WF in the frequency domain of the object (Eq. (10)) and then we propagate the filtered complex amplitude.

The process, shown in Fig. 2, will be applied to flows with different sized particles using an iterative procedure where the object complex amplitude will be sampled using a bench of precomputed Wiener filters. The advantage of this linear filtering approach is especially evident in this case, since the computational cost of the filtering process will be reduced.

3.3. Particle location measurement

We should also address the location of each individual particle once the WF is applied and particles behave ideally as point scatterers.

We will start with a coarse sampling (Fig. 3) where the complex amplitude distribution of the filtered object wave, $U_{oF}(\vec{r})$, is reconstructed at different Z-planes ($\Delta z = 20\mu m$). The reconstructed volume is divided into equally sized parallelepipeds, which we will call a 3D interrogation window (3DIW), where the maximum global intensity is sought. We chose a 3DIW whose dimensions were $20\times20\times100$ pixel^3, which corresponds to $0.0186\times0.0186\times2$mm^3 and extends longer than the capillary z dimension. Pixels in the XY plane are defined by the sensor pixel size and by the magnification, being pixel_x = pixel_y = 0.93μm. Peaks are normalized and they are ordered from higher to lower intensity. Those whose intensity is equal to or less than a certain threshold are discarded.

Even with this initial selection, the remaining peaks may not come from a real particle. We need to ensure these maxima behave as local maxima with a finer sampling of the reconstructed 3DIW as in a PTV algorithm [9].

The filtered object wave is reconstructed around each peak: the complex amplitude is propagated to different planes, with a new Δz = pixel_z =9.8μm. In this case, the 3DIW has an adaptive size in the transverse (XY) plane to take into account the particle defocusing distance from the hologram plane. In the axial direction, the 3DIW is 40 pixel_z (0.392mm) and is centered on the initial position of the maximum. Now, the intensity in the transverse plane (XY) is fitted to a parabolic function, thus obtaining the (X,Y) coordinates of the particle with sub-pixel resolution. The intensity in the longitudinal axis (Z) is adjusted also to a parabola, whose maximum is taken as the particle Z coordinate. The particle is kept in the working set only if the new coordinates and the maximum calculated in the coarse sampling in the transversal direction are close enough. The distance allowed between them depends on different factors, such as the magnification of the system and the size of the particle in the image, but it is of

the order of 1-3 pixels (0.9µm -2.8µm) in the XY plane and of the full range in the Z direction. The correctly identified particles will be tagged and removed from the reconstructed complex amplitude before looking for a new particle.

To define the spatial resolution in the optical axis direction, we proposed in [9] to extrapolate some Particle Image Velocimetry (PIV) concepts related to the accuracy in the velocity measurement. In PIV the in-plane velocity components are obtained from a 2D cross-correlation between 2D interrogation windows. Then, it is assumed that the correlation peak position can be calculated with sub-pixel accuracy by using a three-point estimator [37]. This estimator is usually a Gaussian or a polynomial (parabolic) fit that works best for narrow correlation peaks obtained when the particle image diameter is 3 pixels. In such a case, the accuracy in the measured displacement can be taken as one tenth of the pixel size.

We propose to extend this idea to the particle position measurement as we are using a three-point estimator (a parabolic fit) to obtain the position of the peak produced by the WF filter with sub-pixel accuracy. This peak is big enough to be sampled with several pixels both in the XY plane and along the Z axis. For the (X,Y) coordinates, as pixel_x = pixel_y = 0.93µm, our spatial resolution would be 0.093µm. However, in the holographic reconstruction the sampling along the optical axis is user defined. In order to apply the three-point estimator, we need to establish a pixel_z large enough to ensure that the peak is defined with 2-3 'pixels'. For our experimental parameters (λ, magnification and sensor pixel size), we have found that the intensity of the peak changes significantly when sampled every 10µm. Thus we can assume that the particle position can be measured with subpixel accuracy, ideally, one tenth of the pixel size, i.e. 1µm.

3.4. Scattering planar visualization

The tilted illumination produces tilted particle images i.e., the image of any particle is no longer parallel to the optical axis of the system, but extends along the illumination direction. Figure 4 provides some further insight of the 3D shape of the scattering pattern, showing the central XZ plane of the simulated amplitude for a 24µm disk illuminated with a tilted beam of 10.4° (Fig. 4(a)) and the scattering of a real 24µm particle (Fig. 4(b)). This image is almost identical to the numerical simulation but for some asymmetry and noise, which proves the good performance of our simple particle model.
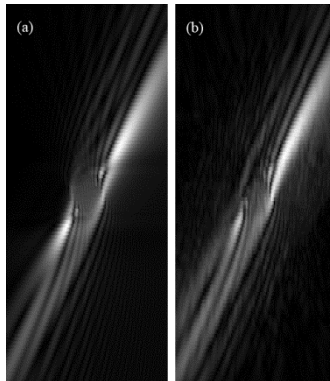

Fig. 4. Central XZ plane of the scattering of a (a) 24µm simulated opaque disk, (b) 24µm particle.

The visualization of a XY or XZ plane gives only partial information of the particle scattering features, being necessary to show more than one plane to have a whole representation, as in Fig. 1(b). We propose visualizing the 3D absolute value of the particle complex amplitude in a 2D image, which we will call Scattering Planar Visualization (SPV). This visualization is similar

to the intensity minimum projection proposed in [13] and with a tilted illumination beam we take full advantage of its characteristics. In order to obtain the SPV we calculate the absolute value of the particle image complex amplitude ($|U_P(x, y, z)|$) in a 3D matrix. Next, at every (x, y) coordinates we search along Z for the maximum amplitude. The SPV is the 2D image obtained as:

$$SPV(x, y) = \max\{|U_P(x, y, z)|, Z\}. \tag{13}$$

Figure 5 shows the SPV calculated for three disks of 3μm, 11μm and 24μm in diameter, in a volume of 119μm×119μm×2mm. The smallest particle (Fig. 5(a)) presents a sharp local maximum in the XY plane and in the optical axis direction, i.e., it behaves as a point scatterer. The SPV for the medium size particle (Fig. 5(b)) shows a symmetrical structure, with two big lobes and two bright points, close together. For the biggest particle (Fig. 5(c)) the SPV shows the two peaks found in Fig. 1(b) at different (x, z) coordinates.
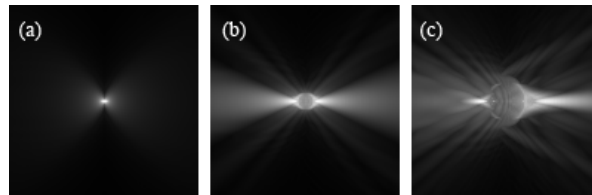

Fig. 5. Scattering Planar Visualization of simulated disks with diameters of: (a) 3μm; (b) 11μm; (c) 24μm.

The SPV shows the scattering features of particles with different sizes, independently of the particle Z-position. Moreover, the SPV allows us to understand, in just one view, why a PTV standard algorithm would find two local maxima, and would wrongly assign them to two different point-like particles. It also shows that the wide and long scattering pattern of multiple particles will mix, which will hinder the correct individual localization in a volume. From now on we are going to use the SPV to show the effect of the Wiener filter on the recorded particle fields.

4. Linear filtering performance and sensitivity

To compute the Wiener Filter described by Eq. (8) we can use either an isolated particle scattering pattern or the simulated scattering of an opaque disk. The filter with the real scattering pattern provides higher peaks but it is very sensitive to the dispersion in size and shape. The result is also affected by the surrounding noise of the chosen particle and by the scattering of the neighboring particles. The filter built with the simulated scattering of an opaque disk produces slightly smaller peaks. However, it has the advantage that it is noiseless, and the radius can be adjusted to the different sizes in the sample, which allows for an iterative and automatic process as the one described in Section 4.2. This filter imposes an extra condition over the particle characteristics: particles should be spherical in order to match the numerical filter. In addition, particles must have a near zero transmittance. The Wiener filtering will provide for good results when opaque particles are used or in those cases where the difference between the refractive index of the particle and that of the surrounding medium is large enough (as bubbles in water). The technique fails when applied to small transparent particles. These act as micro-lenses, focusing the illumination beam in a bright spot, which is the prevalent feature in their scattering pattern and is too similar to the scattering of a punctual particle.

4.1. Linear filtering performance

In Section 3.2, we have described the computational advantage of our method against the method proposed in [31].

Here we are going to compare the performance of both methods. Figure 6(a) shows the SPV of a white cell model, which is identical to the simulated SPV shown in Fig. 5(c). Figure 6(b) shows the resultant SPV of the filtered complex amplitude after applying our linear filtering. Figure 6(c) shows the SPV after applying a non-linear filtering to the hologram intensity as in [31], presented as amplitude to allow comparison. The better performance of the linear filtering is apparent as the SPV shows a sharp peak very similar to that of a point scatterer, as it is shown in Fig. 5(a).
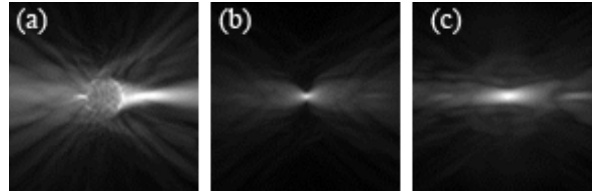

Fig. 6. SPV of a white cell model: (a) original; (b) after applying our linear filtering; (c) after applying a non-linear filtering process.

To quantify the performance of these methods we have calculated the SNR, as the peak value divided by the average intensity in the 3D reconstructed volume. The best SNR is obtained for the 2D complex amplitude filtering approach, Fig. 6(b), with a value of 277, almost double that the SNR obtained for the 3D intensity filtering procedure with a SNR of 143.

4.2. Filter sensitivity

In order to analyze the WF sensitivity we built a bench of filters in which $\tilde{P}(\vec{k})$ was calculated from opaque disks, whose diameter varied from 27µm to 1µm, every 0.5µm, and where β was taken as the 20% of the total intensity of the scattering pattern spectrum. Figure 7 shows the maximum intensity of the resultant particle image after applying these filters to the complex amplitude of three real particles (magnetic, red and white cell model).
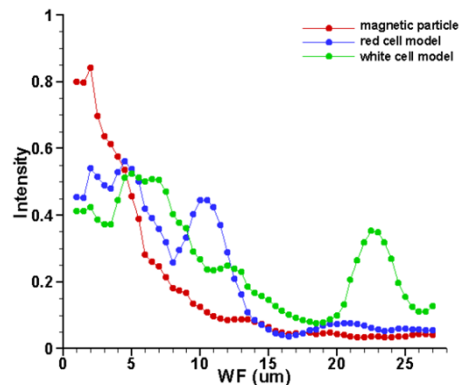

Fig. 7. Maximum intensity measured after applying series of WF to a magnetic particle and to the red and white cell models.

For the white cell model, the filtered intensity shows one well-defined peak at 22.5µm. This peak has a relative intensity of a 35% because the bigger the particles are, the more different the scattering pattern of the particle and the disk is. A broad and irregular peak appears for 5-7µm, as the WF defined for small sizes detects every secondary intensity peak in the particle scattering. These maxima at smaller diameters, which cannot be avoided, determine our particle discrimination strategy.

The same behavior is found for the red cell model, whose main peak is found at 10.5µm. Magnetic particles are small enough to be considered as punctual particles and their scattering do not present secondary peaks (Fig. 5(a)). For this reason, the chosen particle presents only a small peak at 3µm. Let us recall that those values are inside the particle sample tolerance as provided by the manufacturer. Figure 7 also shows the method's high sensitivity: with a magnification M = 7.0, sizes can be detected with an accuracy of less than 0.5 µm.

These results suggest that the optimal way to discriminate particles with different sizes is by means of an iterative process, which will begin by applying the filter built with the $\tilde{P}(\vec{k})$ of the biggest size present in the particle field. The filter will be applied and the filtered reconstructed complex amplitude will be propagated in the search for maxima. Once a maximum is identified as a particle, its complex amplitude will be removed. The process will be repeated by reducing the filter size until reaching the smallest known size in the particle field.

5. Experimental results

5.1. *Wiener filter application in samples with only one particle size*

Results shown in Figs. 8, 9 and 10, correspond to experiments designed ad-hoc for testing the filtering process, in which we injected liquid seeded with only one particle type in the capillary.
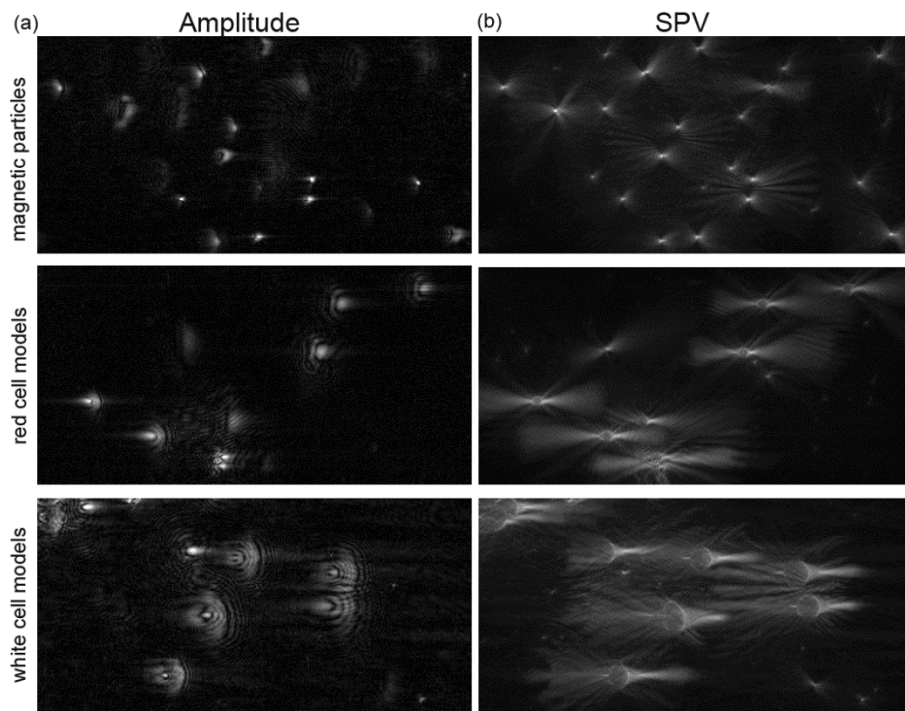

Fig. 8. Reconstructed amplitude of the central XY capillary plane (a) and (b) SPV for magnetic particles (top), red (middle) and white cell model (bottom).

Figure 8(a) shows the amplitude computed in the central XY capillary plane in a region of 512×256 pixels (0.476×0.238mm²) for the three particle types (increasing size from top to bottom). Images are normalized with the illumination beam, so they would be comparable and similar to the obtained in a flux with a mixture of seeders. A few particles can be seen in the images: some of them are in focus; some others are out of focus. Figure 8(b) shows the SPV for the three particle fields, where it is evident that the SPV is independent of the particle axial
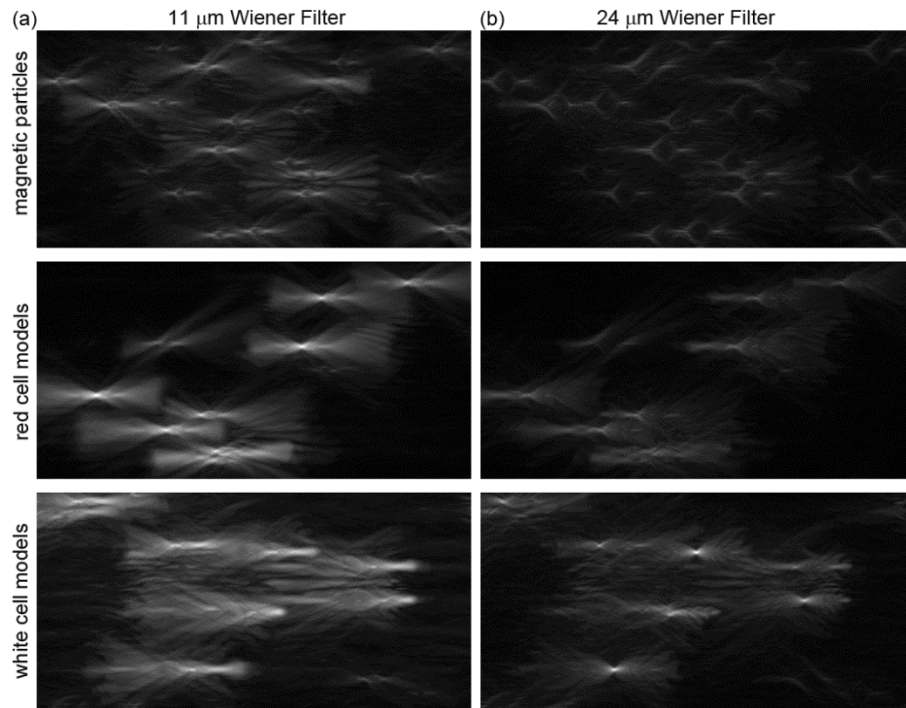
Fig. 9. SPV of the filtered complex amplitude obtained when the (a) 11μm-WF and (b) 24μm-WF are applied to the magnetic (top), red cell model (middle), and white cell model (bottom) particles.
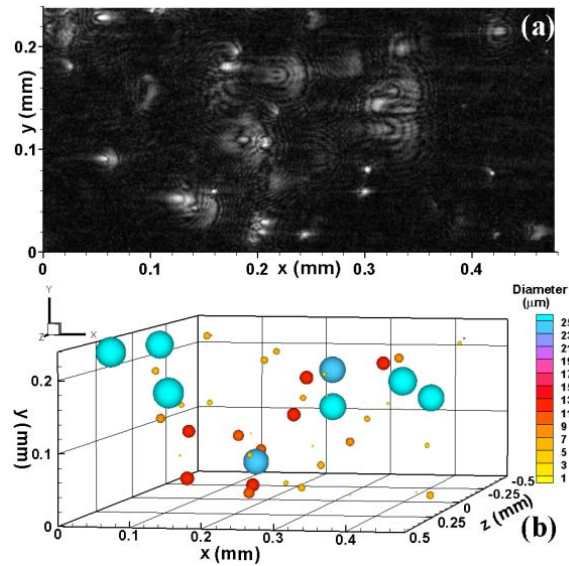

Fig. 10. (a) Summed reconstructed complex amplitude of the central XY capillary plane; (b) measured particle field.

position. Magnetic particles show the characteristic pattern of point scatterers, while the other two present the complex structures shown previously in Fig. 5. In spite of the low concentration, it is evident that the scattering patterns overlap.

The filtering method described in Fig. 2 has been applied to the holograms whose complex amplitude absolute values are shown in Fig. 8. Two WF were applied, in which $\tilde{P}(\vec{k})$ was calculated with the scattering of an opaque disk of 11 and 24μm respectively. Figure 9 shows the SPV of the resulting complex amplitude after applying the 11μm-WF (Fig. 9(a)) and after applying the 24μm-WF (Fig. 9(b)). The effect of the 3μm-WF is negligible in all cases and it is not represented. The small particles nearly behave as point scatterers, subsequently, their WF do not modify the SPV of Fig. 8(b) appreciably.

When these filters are applied to the 3μm particles (Fig. 9, top) we obtain the filter shape, i.e. the particle with which the filter was calculated, as we are correlating the modeled scatterer (the filter) with a particle that is already a delta-like function. When filter and particle size match, the particle SPV turns into the SPV of a point scatterer. Therefore, the 11μm-WF gives an optimum response for the red cells (Fig. 9(a), middle) and the 24μm-WF identifies well the white cells (Fig. 9(b), bottom). Besides, the brightness of each resultant peak changes when scanning the complex amplitude with filters that differs on 1μm (or even 0.5μm), showing the dispersion in size of these samples. This proves the method high sensitivity and its potential accuracy in size determination.

When the filter and the particle do not match, distorted SPV appears with spurious peaks. This can be seen when the 11μm-WF is applied to the white cells (Fig. 9(a), bottom) or the 24μm-WF is applied to the red cells (Fig. 9(b), middle). In this last case, the filtering produces low intensity peaks that can be removed by applying a threshold. These results are consistent with the analysis of the filter performance of section 4.2.

Once the filtering performance was tested, we obtained the sizes of the particles in each one of the reconstructed amplitudes shown in Fig. 8(a). Measured sizes were consistent with the nominal values given by the manufacturers, except for the case of magnetic particles. We found values of 9μm or 10μm, though their nominal size is between 2μm and 4μm. For this reason, we verified looking with a simple microscope that our sample did indeed present particles of these sizes.

In summary, we have found that a Wiener filter computed for a particle size and applied to particles smaller than the defined size produces low intensity peaks that can be removed by applying a threshold. In addition, we have found that if the particle is bigger than the size defined for the Wiener filter, the peaks have enough intensity to be wrongly identified by the PTV algorithms used to locate particles. In consequence, the WF must be applied from bigger to smaller sizes of the disk. These results are consistent with the analysis of the filter performance of section 4.2.

5.2.   *Wiener filter application in a flow with several particle sizes*

In a flow with a mixture of seeders, the process described above can be applied iteratively. To ensure a correct identification of the particles in the sample, the process must start by applying the WF corresponding to the biggest known particles. Once the particles have been identified and removed from the reconstructed amplitude, the analysis is repeated by reducing the filter nominal size iteratively until the smallest size is reached.

The performance of this method was tested by adding the complex amplitudes shown in Fig. 8(a) in one image (Fig. 10(a)). The image was scanned with filters built with the $\tilde{P}(\vec{k})$ of disks whose size varied from 27μm to 2μm, every 1μm.

All the identified particles are shown on the 3D image in Fig. 10(b). The blue particles have been found to be between 27μm to 20μm (white cell model), the medium-sized red circles have diameters from 19μm to 10μm (red cell model) and the rest (with diameters from 9μm to 2μm)

are marked as little yellow circles (magnetic particles). If we compare with the SPV in Fig. 8, we can see that every particle is correctly identified. Even the unintended scatterers (particle contamination or dust) on the flow in Fig. 8(b) (middle and bottom) are identified as small particles. This figure also shows the method good performance when particles with very different sizes have different axial position.

An experiment with the real flow was done with the white cells model and the magnetic particles travelling in the capillary simultaneously, at a flow rate of 0.01ml/min. Holograms were recorded with an exposure time of 1.5ms at 33fps. The system magnification was set to M = 2.3 by using a lens with f'=105mm, and a smaller aperture (9.7×19.3mm²). The capillary recorded length was 7.25mm. The hologram reconstruction and filtering process was done as described previously.

Figure 11 shows the particle field measured in a region of only 180×130 pixels (0.51×0.27mm²). In spite of the increase in the noise and the loss of spatial resolution, inherent to the smaller magnification, the results are very good. All the biggest particles are detected. In addition, some medium size particles are found, which can be related either to spurious contamination of the sample or to the big dispersion in size of the magnetic particles as it was found in previous experiments. There is still some background intensity that our analysis does not associate to real particles. These spurious peaks do not behave as quality local maxima as explained in section 4.2, and they cannot be tracked through the flow.
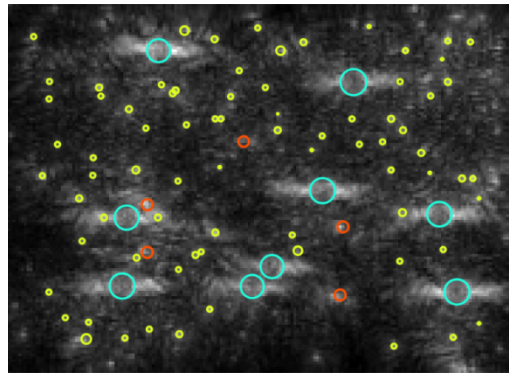

Fig. 11. SPV a real hologram with big particles marked in blue, medium particles in red and small particles in yellow.
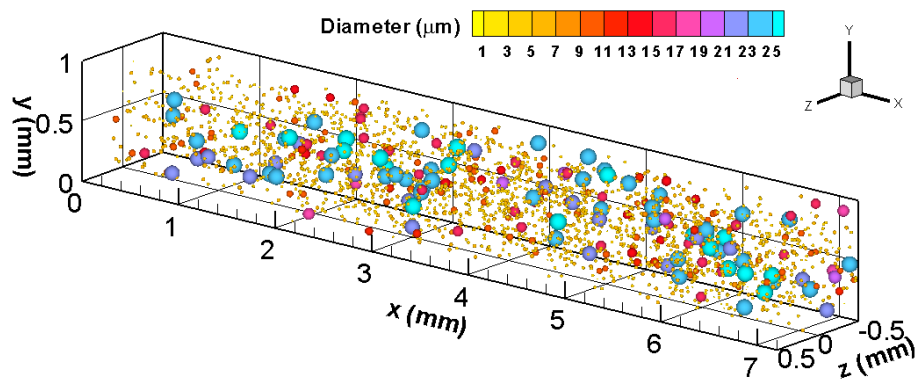

Fig. 12. Measured particle distribution in the recorded capillary length.

The measured 3D particle field in the recorded capillary length is shown in Fig. 12. There have been identified 83 particles between 27 and 20μm, 111 particles between 10 and 19.5μm and 2257 smaller particles, which gives a particle density of 0.0027 ppp.

6. Conclusions

We introduce a new method for measuring the size and position of particles with different characteristics, which can be adapted to any flow and any magnification. This method is based on filtering the reconstructed complex amplitude of in-line holograms by using a Wiener filter. The main advantage of this process, as compared with the reconstructed three-dimensional intensity, lies in the linearity of the filtering process and the complex amplitude reconstruction. Thus, we modify the complex amplitude spectrum before propagating to any plane of a volume, simplifying the process and requiring minimum computational resources. An iterative process has been developed to automate the particle size and position measurement, which can be applied in any particle field. This procedure has been proven in a capillary model where three types of particles, with a broad size range, have been successfully discriminated in different conditions. The method has shown great performance in experiments with two magnification factors (M = 2.3 and 7.0). The sensitivity in the latter case has been found to be better than 0.5 μm.

Disclosures. The authors declare no conflicts of interest.

Data availability. Data underlying the results presented in this paper are not publicly available at this time but may be obtained from the authors upon reasonable request

References

1. M. Ito, H. Shinkai, T. Honda, and Kobayashi, "Medical application of functionalized magnetic nanoparticles," J. Biosci. Bioeng. **100**(1), 1–11 (2005).
2. Q. A. Pankhurst, N. T. K. Thanh, S. K. Jones, and J. Dobson, "Progress in applications of magnetic nanoparticles in biomedicine," J. Phys. D: Appl. Phys. **42**(22), 224001 (2009).
3. N. Pamme, "On-chip bioanalysis with magnetic particles," Curr. Opin. Chem. Biol. **16**(3-4), 436–443 (2012).
4. J. Pallares, "A Criterion for the Complete Deposition of Magnetic Beads on the Walls of Microchannels," PLoS One **11**(3), e0151053 (2016).
5. U. Schnars and W. Jüptner, "Digital recording and numerical reconstruction of holograms," Meas. Sci. Technol. **13**(9), R85–R101 (2002).
6. V. Palero, J. Lobera, P. Brunet, N. Andrés, and M. P. Arroyo, "3D characterization of the inner flow in an oscillating drop," Exp. Fluids **54**(9), 1568 (2013).
7. J. Katz and J. Sheng, "Applications of holography in fluid mechanics and particle dynamics," Annu. Rev. Fluid Mech. **42**(1), 531–555 (2010).
8. P. Memmolo, L. Miccio, M. Paturzo, G. Di Caprio, G. Coppola, P. A. Netti, and P. Ferraro, "Recent advances in holographic 3D particle tracking," Adv. Opt. Photonics **7**(4), 713–755 (2015).
9. A. M. López, J. Lobera, N. Andrés, M. P. Arroyo, V. Palero, I. Sancho, A. Vernet, and J. Pallarés, "Advances in interferometric techniques for the analysis of the three-dimensional flow in a lid-driven cylindrical cavity," Exp. Fluids **61**(1), 10 (2020).
10. G. Pan and H. Meng, "Digital holography for particle fields: reconstruction by use of complex amplitude," Appl. Opt. **42**(5), 827–833 (2003).
11. S. L. Pu, D. Allano, B. Patte-Rouland, M. Malek, D. Lebrun, and K. F. Cen, "Particle field characterization by digital in-line holography: 3D location and sizing," Exp. Fluids **39**(1), 1–9 (2005).
12. C. Hesseling, J. Peinke, and G. Gülker, "Adaptation of reference volumes for correlation based digital holographic particle tracking," Meas. Sci. Technol. **29**(4), 045207 (2018).
13. L. Tian, N. Loomis, J. A. Domínguez-Caballero, and G. Barbastathis, "Quantitative Measurement of Size and Three-Dimensional Position of Fast-Moving Bubbles in Air-Water Mixture Flows Using Digital Holography," Appl. Opt. **49**(9), 1549–1554 (2010).
14. J. Gao, D. R. Guildenbecher, P. L. Reu, and J. Chen, "Uncertainty Characterization of Particle Depth Measurement Using Digital In-Line Holography and the Hybrid Method," Opt. Express **21**(22), 26432 (2013).
15. C. Li, J. Miller, J. Wang, S. S. Koley, and J. Katz, "Size Distribution and Dispersion of Droplets Generated by Impingement of Breaking Waves on Oil Slicks," J. Geophys. Res. Ocean. **122**(10), 7938–7957 (2017).

16. V. Palero, M. Arroyo, and J. Soria, "Digital holography for micro-droplet diagnostics," Exp. Fluids **43**(2-3), 185–195 (2007).
17. O. Bryngdahl and A. Lohmann, "Single-Sideband Holography," J. Opt. Soc. Am. **58**(5), 620–624 (1968).
18. V. Palero, J. Lobera, N. Andrés, and M. P. Arroyo, "Shifted knife-edge aperture digital in-line holography for fluid velocimetry," Opt. Lett. **39**(11), 3356–3359 (2014).
19. C. Ramirez, A. Lizana, C. Iemmi, and J. Campos, "Inline digital holographic movie based on a double-sideband filter," Opt. Lett. **40**(17), 4142–4145 (2015).
20. J. Lobera, V. Palero, E. M. Roche, M. Gómez-Climente, A. M. López-Torres, N. Andrés N, and M. P. Arroyo, "Tilted illumination in-line holographic velocimetry: Improvements in the axial spatial resolution," Opt. Lasers Eng. **134**, 106280 (2020).
21. T. Ooms, W. Koek, and J. Westerweel, "Digital holographic particle image velocimetry: eliminating a sign-ambiguity error and a bias error from the measured particle field displacement," Meas. Sci. Technol. **19**(7), 074003 (2008).
22. J. Lu, J. P. Fugal, H. Nordsiek, E. W. Saw, R. A. Shaw, and W. Yang, "Lagrangian particle tracking in three dimensions via single-camera in-line digital holography," New J. Phys. **10**(12), 125013 (2008).
23. T. Dracos, "Particle Tracking Velocimetry (PTV)," in *Three-Dimensional Velocity and Vorticity Measuring and Image Analysis Techniques*, (Springer, 1996).
24. H.C. van de Hulst, *Light scattering by small particles*, (Chapman and Hall, 1957).
25. B. Javidi, "Generalization of the linear matched filter concept to nonlinear matched filters," Appl. Opt. **29**(8), 1215–1224 (1990).
26. J. Khoury, P. D. Gianino, and C. L. Woods, "Wiener-like correlation filters," Appl. Opt. **39**(2), 231–237 (2000).
27. V. K. V. Kumar and Z. Bahri, "Phase-only filters with improved signal to noise ratio," Appl. Opt. **28**(2), 350 (1989).
28. T. Kim, "Optical sectioning by optical scanning holography and a Wiener filter," Appl. Opt. **45**(5), 872–879 (2006).
29. J. L. Horner and P. D. Gianino, "Phase-only matched filtering," Appl. Opt. **23**(6), 812–816 (1984).
30. J. Lobera and J. M. Coupland, "Optical diffraction tomography in fluid velocimetry: the use of a priori information," Meas. Sci. Technol. **19**(7), 074013 (2008).
31. T. Latychevskaia, F. Gehri, and H. W. Fink, "Depth-resolved holographic reconstructions by three-dimensional deconvolution," Opt. Express **18**(21), 22527–22544 (2010).
32. M. Gómez Climente, J. Lobera, V. Palero, and M. P. Arroyo, "Matched filter applied to discriminate particles with different sizes in biological flows," Proc. SPIE **11060**, 11060 (2019).
33. M. Born and E. Wolf, *Principles of Optics: Electromagnetic Theory of Propagation, Interference and Diffraction of Light*, (Cambridge University Press, 1999).
34. J. M. Coupland and J. Lobera, "Holography, tomography and 3D microscopy as linear filtering operations," Meas. Sci. Technol. **19**(7), 074012 (2008).
35. J. Lobera and J. M. Coupland, "Contrast enhancing techniques in digital holographic microscopy," Meas. Sci. Technol. **19**(2), 025501 (2008).
36. J. W. Goodman, *Introduction to Fourier optics*, (McGraw-Hill Series in Electrical and Computer Engineering, 1996).
37. M. Raffel, C. Willert, S. Wereley, and J. Kompenhans, *Particle Image Velocimetry, a practical guide*, (Springer Verlag, 2007).